Pergamon

Modeling three-dimensional solidification with magnetic fields and reduced gravity

GEORGE S. DULIKRAVICH and VINEET AHUJA

Department of Aerospace Engineering, 233 Hammond Building, The Pennsylvania State University, University Park, PA 16802, U.S.A.

and

SEUNGSOO LEE

Agency for Defense Development, Taejon, Korea

Abstract—Two interacting systems of partial differential equations governing three-dimensional laminar flow of an incompressible viscous fluid undergoing solidification or melting while under the influence of an externally applied magnetic field have been formulated and integrated numerically. The model includes effects of Joule heating, latent heat, and arbitrary magnitude and orientation of gravity and the magnetic field. It allows for arbitrary temperature-dependent physical properties within the melt and the solid phase. The mushy region is captured by varying viscosity orders of magnitude in the mushy region and by allowing latent heat of phase change to be an arbitrary function of temperature. The uniqueness of this approach is in the fact that both liquid and solid phases are treated as incompressible liquids with the solid phase having an extremely high viscosity. It was found numerically that the magnetic field strength and orientation can significantly influence flow field velocity and vorticity, amount of accrued solid, and the solid/liquid interface shape.

INTRODUCTION

THE OBJECTIVE of this paper is to elaborate on a mathematical model and an accompanying numerical algorithm capable of simulating fully three-dimensional melt flow control during melting and solidification via an arbitrarily distributed and oriented externally applied magnetic field. It has been well known analytically [1, 2] and demonstrated computationally [3–12] that the magnetic field can eliminate vorticity from the flow field and reduce the magnitude of the fluid motion so that the solid/liquid front shape and its propagation speed could be manipulated. The formulation presented in this paper extrapolates on our previous work [6–12] which was based on the fundamental concepts of MagnetoHydroDynamics (MHD) as formulated by Stuetzer [2] and an extended Boussinesq approximation formulation [13] that allows for temperature-dependent physical properties. Our formulation simultaneously predicts detailed velocity, pressure, temperature and magnetic fields for the moving melt, while capturing the forming solid phase by using a single computer code. The same mathematical formulation and computer code can simulate the reverse process of melting of the solid phase. In this work we have formulated the entire problem as three-dimensional and time-dependent although our computational results will be for steady situations only. The objective is to develop a consistent mathematical model and an accompanying computer code for detailed analysis of MHD solidification and melt-

ing in general three-dimensional configurations in terrestrial conditions and in reduced gravity. Our formulation is simultaneously applicable to regions containing all melt, all solid, or their mixture (mushy region). We modeled the locally solid regions as containing the melt having extremely high viscosity. Consequently, the computed velocities in the solid regions will not be identically zero, but will be extremely small compared to the velocities in the melt. In this work, only incompressible flow will be considered while accounting for thermal buoyancy via an extended Boussinesq approximation in the form which is valid even when melt [13] and solid properties vary as separate arbitrary functions of non-dimensional temperature [9–12]. To account for this, we present a more complete and consistent mathematical model for MHD solidification than we did in our earlier publications [6–12].

MODELING MHD SOLIDIFICATION

Starting with Maxwell's equations and Ohm's law, the magnetic field transport equation can be derived [1, 2] as

$$\frac{\partial \mathbf{H}}{\partial t} - \nabla \times (\mathbf{v} \times \mathbf{H}) = -\frac{1}{\rho \gamma \sigma} \nabla^2 \mathbf{H}. \qquad (1)$$

For many applications involving parametric studies it is convenient to use non-dimensional temperature, $\theta = (T - T_0)/\Delta T_0$. Typically, either $\Delta T_0 = T_{\text{liquidus}} -$

NOMENCLATURE

c specific heat [J kg^{-1} K^{-1}]
Ec Eckert number
f volume fraction of the melt in a computational cell
Fr Froude number
$\mathbf{g}(g_x, g_y, g_z)$ gravity force per unit volume [m s^{-2}]
Gr Grashof number
$\mathbf{H}(H_x, H_y, H_z)$ magnetic field [H kg^{-1}]
Ht Hartmann number
k heat conductivity coefficient [W m^{-1} K^{-1}]
l length [m]
L latent heat of liquid/solid phase change [J kg^{-1}]
p pressure [kg m^{-1} s^{-2}]
P_m magnetic Prandtl number
Pr Prandtl number
Ra Rayleigh number, $Gr\ Pr$
Re hydrodynamic Reynolds number
S_{te} Stefan number
t time [s]
T absolute temperature [K]
ΔT_0 reference temperature difference [K]
$\mathbf{v}(u, v, w)$ velocity vector [m s^{-1}]
V volume [m^3]
x, y, z Cartesian coordinates [m].

Greek symbols

α thermal expansion coefficient [K^{-1}]

β artificial compressibility parameter
γ magnetic permeability coefficient [H m^{-1}]
μ viscosity coefficient [kg m^{-1} s^{-1}]
ξ, η, ζ non-orthogonal grid coordinates
ρ density [kg m^{-3}]
σ electrical conductivity [Ω^{-1} m^{-1}]
θ non-dimensional temperature
ϕ gravity potential.

Subscripts

0   reference value
cold   cold wall
hot   hot wall
i component of a vector
j component of a vector
l   liquid
liquidus   liquidus temperature condition
p   specified
s   solid
solidus   solidus temperature condition
,   differentiation.

Superscripts

l   liquid
s   solid
T   transpose of a matrix or a vector
*   nondimensional values
'   function of non-dimensional temperature.

$T_{solidus}$ and $T_0 = T_{solidus}$ or $\Delta T_0 = T_{hot} - T_{cold}$ and $T_0 = T_{cold}$. The latent heat released or absorbed per unit mass of mushy region (where $T_{liquidus} > T > T_{solidus}$) is proportional to the local volumetric liquid/(liquid + solid) ratio often modeled [14] as

$$f = \frac{V_l}{V_l + V_s} = \left(\frac{\theta - \theta_{solidus}}{\theta_{liquidus} - \theta_{solidus}}\right)^n \qquad (2)$$

where the exponent n is typically $0.2 < n < 5$. For certain materials their physical properties (density, viscosity, heat conductivity and heat capacity) can be significantly different in the melt as compared to its solid phase. We will assume linear variation of density as a function of non-dimensional temperature in the liquid and in the solid

$$\rho_l' = 1 + \frac{\partial(\rho_l/\rho_{0l})}{\partial T}\bigg|_0 (T - T_0)$$

$$= 1 + \frac{\partial(\rho_l/\rho_{0l})}{\partial \theta}\bigg|_0 (\theta - \theta_0)$$

$$= 1 - \alpha_{0l}^*(\theta - \theta_0) \qquad (3)$$

with a similar expression for the solid phase. The partial differential equations governing fluid flow (Navier–Stokes) and the magnetic field transport (Maxwell) can be non-dimensionalized in a number of ways. If the flow has a mean stream, the non-dimensionalization will lead to the introduction of the hydrodynamic Reynolds number because of the well-defined reference velocity. Thus,

$$\mathbf{v}^* = \frac{\mathbf{v}}{|\mathbf{v}_0|} \quad \mathbf{g}^* = \frac{\mathbf{g}}{|\mathbf{g}_0|} \quad \mathbf{H}^* = \frac{\mathbf{H}}{|\mathbf{H}_0|}$$

$$\mathbf{x}^* = \frac{\mathbf{x}}{l_0} \quad t^* = \frac{t|\mathbf{v}_0|}{l_0} \quad p^* = \frac{p}{\rho_0|\mathbf{v}_0|^2} \qquad (4)$$

$$\rho_l^* = \frac{\rho_{0l}}{\rho_0}\rho_l' \quad \mu_l^* = \frac{\mu_{0l}}{\mu_0}\mu_l' \quad k_l^* = \frac{k_{0l}}{k_0}k_l'$$

$$c_l^* = \frac{c_{0l}}{c_0}c_l' \quad a_l^* = \frac{\alpha_{0l}}{\alpha_0}\alpha_l' \qquad (5)$$

with similar expressions for the solid phase. In this work we assumed that σ and γ do not vary with temperature ($\sigma_l^* = \sigma_{0l}/\sigma_0$, $\sigma_s^* = \sigma_{0s}/\sigma_0$, $\gamma_l^* = \gamma_{0l}/\gamma_0$ and $\gamma_s^* = \gamma_{0s}/\gamma_0$). Thus, the reference values des-

ignated with the subscript '0' are arbitrary. Then

$$Re = \frac{\rho_0 v_0 l_0}{\mu_0} \quad Fr^2 = \frac{|v_0|^2}{|g_0| l_0} \quad Ec = \frac{|v_0|^2}{c_0 \Delta T_0} \quad (6)$$

$$Pr = \frac{\mu_0 c_0}{k_0} \quad S_{te} = \frac{c_0 \Delta T_0}{L_0} \quad P_m = \frac{\gamma_0 \sigma_0 \mu_0}{\rho_0} \quad (7)$$

$$Gr = \frac{\rho_0^2 \alpha_0 |g_0| \Delta T_0 l_0^3}{\mu_0^2} \quad Ht = \gamma_0 l_0 |H_0| \left(\frac{\sigma_0}{\mu_0}\right)^{1/2}. \quad (8)$$

Then, adopting an extended Boussinesq approximation [13] to MHD flows, the non-dimensional Navier–Stokes equations for phase-changing mixtures of two liquids become:

Mass conservation for two-phase MHD flows

$$\nabla^* \cdot v^* = 0. \quad (9)$$

Linear momentum conservation for two-phase MHD flows with thermal buoyancy and magnetic force

$$\tilde{\rho} \frac{\partial v^*}{\partial t^*} + f \rho_l^* \nabla^* \cdot (v^* v^* + \bar{p}_l^* I)$$

$$+ (1-f)\rho_s^* \nabla^* \cdot (v^* v^* + \bar{p}_s^* I)$$

$$= f \left[\nabla^* \cdot \left(\frac{\mu_l^*}{Re} (\nabla^* v^* + (\nabla^* v^*)^T)\right) \right.$$

$$+ \rho_l^* \gamma_l^* \frac{Ht^2}{P_m Re^2} (\nabla^* \times H^*) \times H^* + \rho_l^* \alpha_l^* \frac{Gr \theta}{Re^2} g^* \right]$$

$$+ (1-f)\left[\nabla^* \cdot \left(\frac{\mu_s^*}{Re} (\nabla^* v^* + (\nabla^* v^*)^T)\right) \right.$$

$$+ \rho_s^* \gamma_s^* \frac{Ht^2}{P_m Re^2} (\nabla^* \times H^*) \times H^* + \rho_s^* \alpha_s^* \frac{Gr \theta}{Re^2} g^* \right]. \quad (10)$$

Energy conservation for incompressible two-phase MHD flows including Joule heating

$$(f \rho_l^* (c_{el}^* \theta)_{,\theta} + (1-f)\rho_s^* (c_{es}^* \theta)_{,\theta}) \frac{\partial \theta}{\partial t^*}$$

$$+ f \rho_l^* \nabla^* \cdot (c_{el}^* \theta v^*) + (1-f)\rho_s^* \nabla^* \cdot (c_{es}^* \theta v^*)$$

$$= f \left(\frac{1}{Re Pr} \nabla^* \cdot (k_l^* \nabla^* \theta)\right.$$

$$+ \frac{\gamma_l^*}{\sigma_l^*} \frac{Ht^2 Ec}{P_m^2 Re^3} (\nabla^* \times H^*) \cdot (\nabla^* \times H^*)\right)$$

$$+ (1-f)\left(\frac{1}{Re Pr} \nabla^* \cdot (k_s^* \nabla^* \theta)\right.$$

$$+ \frac{\gamma_s^*}{\sigma_s^*} \frac{Ht^2 Ec}{P_m^2 Re^3} (\nabla^* \times H^*) \cdot (\nabla^* \times H^*)\right) \quad (11)$$

where the subscripts after the comma designate partial differentiation with respect to the variable or variables that follow the comma.

The magnetic field transport equations for the two-phase MHD flow in their non-dimensional form become

$$\frac{\partial H^*}{\partial t^*} - \nabla^* \times (v^* \times H^*)$$

$$= \frac{f/(\sigma_l^* \gamma_l^*) + (1-f)/(\sigma_s^* \gamma_s^*)}{P_m Re \tilde{\rho}} \nabla^{*2} H^*. \quad (12)$$

Here $\tilde{\rho} = f \rho_l^* + (1-f)\rho_s^*$, while $f = 1$ for $\theta > \theta_{liquidus}$ and $f = 0$ for $\theta < \theta_{solidus}$. Non-dimensional hydrostatic, hydrodynamic, and magnetic pressures were combined to give

$$\bar{p}_l^* = \frac{p^*}{\rho_l^*} + \frac{\phi^*}{Fr^2} + \frac{\gamma_l^* Ht^2}{P_m Re^2} H^* \cdot H^*$$

$$\bar{p}_s^* = \frac{p^*}{\rho_s^*} + \frac{\phi^*}{Fr^2} + \frac{\gamma_s^* Ht^2}{P_m Re^2} H^* \cdot H^* \quad (13)$$

where ϕ^* is the non-dimensional gravity potential defined as $g^* = \nabla^* \phi^*$. We used an enthalpy method to formulate the equivalent specific heat coefficients in the liquid and the solid phases to give

$$c_{el}^* = c_l^* - \frac{1}{S_{te}} \frac{\partial f}{\partial \theta} \quad \text{and} \quad c_{es}^* = c_s^* - \frac{1}{S_{te}} \frac{\partial f}{\partial \theta},$$

respectively. Notice that this expression allows for the latent heat not to be a constant, but to be released in the mushy region according to the empirical law given in equation (2).

NUMERICAL MODEL FOR MHD SOLIDIFICATION

For clarity of presentation, we will drop the asterisk symbol in all future formulas. Equations (9)–(12) represent a system of eight coupled non-linear partial differential equations. This global system has been split into two systems in order to simplify computer programming [6]. The first system represents the non-dimensional Navier–Stokes equations for incompressible flows with thermal buoyancy, magnetic field effects and possible solidification or melting. It can be written in a fully conservative form in terms of the non-orthogonal grid-following boundary-fitted coordinate system as

$$\bar{D}_{NS} \frac{\partial \tilde{Q}_{NS}^l}{\partial t} + f \rho_l^* \left(\frac{\partial \tilde{E}_{NS}^l}{\partial \xi} + \frac{\partial \tilde{F}_{NS}^l}{\partial \eta} + \frac{\partial \tilde{G}_{NS}^l}{\partial \zeta}\right)$$

$$+ (1-f)\rho_s^* \left(\frac{\partial \tilde{E}_{NS}^s}{\partial \xi} + \frac{\partial \tilde{F}_{NS}^s}{\partial \eta} + \frac{\partial \tilde{G}_{NS}^s}{\partial \zeta}\right)$$

$$= f \left(\frac{\partial}{\partial \xi}\left(\frac{\tilde{D}_{NS}^l}{J} g_{ij} \frac{\partial J \tilde{Q}_{NS}^l}{\partial \xi}\right) + \frac{\partial}{\partial \eta}\left(\frac{\tilde{D}_{NS}^l}{J} g_{ij} \frac{\partial J \tilde{Q}_{NS}^l}{\partial \eta}\right)\right.$$

$$+ \frac{\partial}{\partial \zeta}\left(\frac{\tilde{D}_{NS}^l}{J} g_{ij} \frac{\partial J \tilde{Q}_{NS}^l}{\partial \zeta}\right)\right)$$

$$+ (1-f)\left(\frac{\partial}{\partial \xi}\left(\frac{\tilde{D}_{NS}^s}{J} g_{ij} \frac{\partial J \tilde{Q}_{NS}^s}{\partial \zeta}\right)\right.$$

$$+ \frac{\partial}{\partial \eta}\left(\frac{\tilde{D}_{NS}^s}{J} g_{ij} \frac{\partial J \tilde{Q}_{NS}^s}{\partial \eta}\right) + \frac{\partial}{\partial \zeta}\left(\frac{\tilde{D}_{NS}^s}{J} g_{ij} \frac{\partial J \tilde{Q}_{NS}^s}{\partial \zeta}\right)\right)$$

$$+ \tilde{S}_{NS}^l + \tilde{S}_{NS}^s \quad (14)$$

where $\xi = \xi(x, y, z)$, $\eta = \eta(x, y, z)$, $\zeta = \zeta(x, y, z)$, $\tilde{\mathbf{Q}}_{NS}$ is the transformed solution vector, $\tilde{\mathbf{E}}_{NS}$, $\tilde{\mathbf{F}}_{NS}$ and $\tilde{\mathbf{G}}_{NS}$ are the transformed flux vectors, and $\tilde{\mathbf{S}}_{NS}$ are the transformed source vectors. Their superscripts l and s designate liquid and solid phase, respectively, so that

$$\bar{\mathbf{D}}_{NS} = \text{diag}\,[\bar{\rho}\bar{\rho}\bar{\rho}\bar{\rho}(f\rho_l^*(c_{cl}^*\theta)_{,\theta} + (1-f)\rho_s^*(c_{cs}^*\theta)_{,\theta})]$$

$$\tag{15}$$

$$\tilde{\mathbf{D}}_{NS}^l = \text{diag}\left[0\;\frac{\mu_l^*}{Re}\;\frac{\mu_l^*}{Re}\;\frac{\mu_l^*}{Re}\;\frac{k_l^*}{Re\,Pr}\right]$$

$$\tilde{\mathbf{D}}_{NS}^s = \text{diag}\left[0\;\frac{\mu_s^*}{Re}\;\frac{\mu_s^*}{Re}\;\frac{\mu_s^*}{Re}\;\frac{k_s^*}{Re\,Pr}\right].\tag{16}$$

Here, $J = \det\,[(\partial(\xi,\eta,\zeta)/\partial(x, y, z))]$ is the determinant of the Jacobian geometric transformation matrix. The metric tensor components are defined as

$$g_{ij} = \frac{\partial\bar{x}_i}{\partial\hat{x}_j}\frac{\partial\bar{x}_j}{\partial\hat{x}_i}.\tag{17}$$

Here, $\bar{x}_i = \bar{x}_i(x, y, z)$ is the Cartesian coordinate vector and $\hat{x}_i = \hat{x}_i(\xi, \eta, \zeta)$ is the curvilinear coordinate vector. The contravariant components U, V, W and $\hat{H}_\xi$, $\hat{H}_\eta$, $\hat{H}_\zeta$ are defined as

$$\begin{Bmatrix} U \\ V \\ W \end{Bmatrix} = \begin{bmatrix} \xi_{,x} & \xi_{,y} & \xi_{,z} \\ \eta_{,x} & \eta_{,y} & \eta_{,z} \\ \zeta_{,x} & \zeta_{,y} & \zeta_{,z} \end{bmatrix}\begin{Bmatrix} u \\ v \\ w \end{Bmatrix}$$

$$\begin{Bmatrix} \hat{H}_\xi \\ \hat{H}_\eta \\ \hat{H}_\zeta \end{Bmatrix} = \begin{bmatrix} \xi_{,x} & \xi_{,y} & \xi_{,z} \\ \eta_{,x} & \eta_{,y} & \eta_{,z} \\ \zeta_{,x} & \zeta_{,y} & \zeta_{,z} \end{bmatrix}\begin{Bmatrix} H_x \\ H_y \\ H_z \end{Bmatrix}.\tag{18}$$

The system of equations (9)–(12) is singular since there is no time derivative term in the mass conservation equation and the system cannot be integrated simultaneously. Consequently, an artificial compressibility [16] term is added to the mass conservation so that

$$\tilde{\mathbf{Q}}_{NS} = \frac{1}{J}\left\{\frac{p}{\beta}\,u\,v\,w\,\theta\right\}^T.\tag{19}$$

Here, β is a user specified parameter that depends on the problem geometry, grid, flow parameters, etc. [17]. In the steady state limit, the time variation of $\tilde{Q}_{NS1}$ term tends to zero and does not influence the accuracy of the steady state solution. For the liquid phase of the Navier–Stokes equations,

$$\tilde{\mathbf{E}}_{NS}^l = \frac{1}{J}\begin{Bmatrix} U \\ Uu+\xi_{,x}\bar{p}_l^* \\ Uv+\xi_{,y}\bar{p}_l^* \\ Uw+\xi_{,z}\bar{p}_l^* \\ c_{cl}^*U\theta \end{Bmatrix}\quad \tilde{\mathbf{F}}_{NS}^l = \frac{1}{J}\begin{Bmatrix} V \\ Vu+\eta_{,x}\bar{p}_l^* \\ Vv+\eta_{,y}\bar{p}_l^* \\ Ww+\eta_{,z}\bar{p}_l^* \\ c_{cl}^*V\theta \end{Bmatrix}$$

$$\tilde{\mathbf{G}}_{NS}^l = \frac{1}{J}\begin{Bmatrix} W \\ Wu+\zeta_{,x}\bar{p}_l^* \\ Wv+\zeta_{,y}\bar{p}_l^* \\ Ww+\zeta_{,z}\bar{p}_l^* \\ c_{cl}^*W\theta \end{Bmatrix}.\tag{20}$$

The non-zero components of the source vector $\tilde{\mathbf{S}}_{NS}^l$ are

$$\tilde{\mathbf{S}}_{NS2}^l = \rho_l^*\left(\frac{\gamma_l^*Ht^2}{P_m\,Re^2}\left(\frac{\partial}{\partial\xi}\left(\frac{\hat{H}_\xi H_x}{J}\right) + \frac{\partial}{\partial\eta}\left(\frac{\hat{H}_\eta H_x}{J}\right)\right.\right.$$
$$\left.\left. + \frac{\partial}{\partial\zeta}\left(\frac{\hat{H}_\zeta H_x}{J}\right)\right) - \frac{\alpha_l^*\,Gr\,\theta}{J\,Re^2}\,g_x\right)\tag{21}$$

$$\tilde{\mathbf{S}}_{NS3}^l = \rho_l^*\left(\frac{\gamma_l^*Ht^2}{P_m\,Re^2}\left(\frac{\partial}{\partial\xi}\left(\frac{\hat{H}_\xi H_y}{J}\right) + \frac{\partial}{\partial\eta}\left(\frac{\hat{H}_\eta H_y}{J}\right)\right.\right.$$
$$\left.\left. + \frac{\partial}{\partial\zeta}\left(\frac{\hat{H}_\zeta H_y}{J}\right)\right) - \frac{\alpha_l^*\,Gr\,\theta}{J\,Re^2}\,g_y\right)\tag{22}$$

$$\tilde{\mathbf{S}}_{NS4}^l = \rho_l^*\left(\frac{\gamma_l^*Ht^2}{P_m\,Re^2}\left(\frac{\partial}{\partial\xi}\left(\frac{\hat{H}_\xi H_z}{J}\right) + \frac{\partial}{\partial\eta}\left(\frac{\hat{H}_\eta H_z}{J}\right)\right.\right.$$
$$\left.\left. + \frac{\partial}{\partial\zeta}\left(\frac{\hat{H}_\zeta H_z}{J}\right)\right) - \frac{\alpha_l^*\,Gr\,\theta}{J\,Re^2}\,g_z\right)\tag{23}$$

$$\tilde{\mathbf{S}}_{NS5}^l = J\frac{\gamma_l^*Ht^2Ec}{\sigma_l^*P_m^2\,Re^3}\,(\tilde{P}_1^2 + \tilde{P}_2^2 + \tilde{P}_3^2).\tag{24}$$

Here,

$$\tilde{P}_1 = \frac{\partial}{\partial\xi}\left(\frac{H_z\xi_{,y} - H_y\xi_{,z}}{J}\right) + \frac{\partial}{\partial\eta}\left(\frac{H_z\eta_{,y} - H_y\eta_{,z}}{J}\right)$$
$$+ \frac{\partial}{\partial\zeta}\left(\frac{H_z\zeta_{,y} - H_y\zeta_{,z}}{J}\right)\tag{25}$$

$$\tilde{P}_2 = \frac{\partial}{\partial\xi}\left(\frac{H_x\xi_{,z} - H_z\xi_{,x}}{J}\right) + \frac{\partial}{\partial\eta}\left(\frac{H_x\eta_{,z} - H_z\eta_{,x}}{J}\right)$$
$$+ \frac{\partial}{\partial\zeta}\left(\frac{H_x\zeta_{,z} - H_z\zeta_{,x}}{J}\right)\tag{26}$$

$$\tilde{P}_3 = \frac{\partial}{\partial\xi}\left(\frac{H_y\xi_{,x} - H_x\xi_{,y}}{J}\right) + \frac{\partial}{\partial\eta}\left(\frac{H_y\eta_{,x} - H_x\eta_{,y}}{J}\right)$$
$$+ \frac{\partial}{\partial\zeta}\left(\frac{H_y\zeta_{,x} - H_x\zeta_{,y}}{J}\right).\tag{27}$$

Generalized vectors $\tilde{\mathbf{Q}}_{NS}^s$, $\tilde{\mathbf{E}}_{NS}^s$, $\tilde{\mathbf{F}}_{NS}^s$, $\tilde{\mathbf{G}}_{NS}^s$ for the solid phase of the Navier–Stokes equations are defined in the same way except that the subscript and the superscript l becomes s.

Similarly, the transformed system of magnetic field transport equations can be expressed as

$$\frac{\partial\tilde{\mathbf{Q}}_{MAG}}{\partial t} + \frac{\partial\tilde{\mathbf{E}}_{MAG}}{\partial\xi} + \frac{\partial\tilde{\mathbf{F}}_{MAG}}{\partial\eta} + \frac{\partial\tilde{\mathbf{G}}_{MAG}}{\partial\zeta}$$

$$= \frac{\partial}{\partial\xi}\left(\frac{\tilde{\mathbf{D}}_{MAG}}{J}\,g_{ij}\,\frac{\partial J\tilde{\mathbf{Q}}_{MAG}}{\partial\xi}\right) + \frac{\partial}{\partial\eta}\left(\frac{\tilde{\mathbf{D}}_{MAG}}{J}\,g_{ij}\,\frac{\partial J\tilde{\mathbf{Q}}_{MAG}}{\partial\eta}\right)$$

$$+ \frac{\partial}{\partial\zeta}\left(\frac{\tilde{\mathbf{D}}_{MAG}}{J}\,g_{ij}\,\frac{\partial J\tilde{\mathbf{Q}}_{MAG}}{\partial\zeta}\right) + \tilde{\mathbf{S}}_{MAG}\tag{28}$$

where the solution vector $\tilde{\mathbf{Q}}_{MAG}$ and the flux vectors $\tilde{\mathbf{E}}_{MAG}$, $\tilde{\mathbf{F}}_{MAG}$, $\tilde{\mathbf{G}}_{MAG}$ are defined as

$$\tilde{\mathbf{Q}}_{\text{MAG}} = \frac{1}{J}\begin{Bmatrix} H_x \\ H_y \\ H_z \end{Bmatrix} \quad \tilde{\mathbf{E}}_{\text{MAG}} = \frac{1}{J}\begin{Bmatrix} H_xU-u\hat{H}_\xi \\ H_yU-v\hat{H}_\xi \\ H_zU-w\hat{H}_\xi \end{Bmatrix} \quad (29)$$

$$\tilde{\mathbf{F}}_{\text{MAG}} = \frac{1}{J}\begin{Bmatrix} H_xV-u\hat{H}_\eta \\ H_yV-v\hat{H}_\eta \\ H_zV-w\hat{H}_\eta \end{Bmatrix} \quad \hat{\mathbf{G}}_{\text{MAG}} = \frac{1}{J}\begin{Bmatrix} H_xW-u\hat{H}_\zeta \\ H_yW-v\hat{H}_\zeta \\ H_zW-w\hat{H}_\zeta \end{Bmatrix}$$

$$(30)$$

while

$$\tilde{\mathbf{D}}_{\text{MAG}} = \frac{f/(\sigma_l^*\gamma_l^*)+(1+f)/(\sigma_s^*\gamma_s^*)}{P_m\,Re\,(f\rho_l^*+(1-f)\rho_s^*)}\mathbf{I} \quad (31)$$

and $\tilde{\mathbf{S}}_{\text{MAG}} = 0$. In the case of a three-dimensional MHD problem, eight partial differential equations need to be satisfied simultaneously. This was accomplished by integrating a system of five fluid flow equations (equation (14)) and a system of three magnetic field equations (equation (28)) in an alternating fashion [6] and after each iteration transferring the information through source-like terms $\tilde{\mathbf{S}}_{\text{NS}}$. By adding the artificially time-dependent term in the mass conservation, the entire Navier–Stokes system becomes non-singular and of a hyperbolic type so that it can be integrated in time using an artificial time maching [6] technique based on an explicit four-stage Runge–Kutta time-stepping algorithm [18]. The explicit time integration scheme was used because it can be efficiently vectorized and easily modified when additional equations need to be incorporated in a system. A small amount of fourth order artificial dissipation [18] was added to the Navier–Stokes system at higher Reynolds number flows to suppress numerical oscillations that appear due to even–odd decoupling caused by central space differencing.

BOUNDARY CONDITIONS

Solid wall boundary conditions

Along the solid walls, the velocity components were set to zero. The pressure gradient normal to the walls calculated from the momentum equations were used to compute pressure at the solid boundaries. This gives physically correct wall pressure distribution rather than assuming zero pressure gradient normal to the wall. Depending on which type of thermal boundary condition was imposed at the wall, the wall temperature was either specified or obtained from the specified surface heat flux and the temperatures computed at the points on the first grid line off the boundary. When the wall is a perfect electric conductor, the tangential component of the magnetic field is discontinuous while the normal component is continuous. If $\langle\ \rangle$ denotes the jump across the boundary, then at the wall boundary $\mathbf{n}\cdot\mathbf{H} = 0$. If the wall is a perfect electric insulator the magnetic field will have no discontinuity at the wall, that is $\langle\mathbf{H}\rangle = 0$.

Characteristic inlet and exit boundary conditions

In the case of a melt flow through a three-dimensional passage with an open inlet and an exit, both characteristic and non-reflective boundary conditions have been implemented in our formulation. Characteristic treatment of inlet and exit flow boundary conditions [6] can be formulated by rewriting the system (14) in a non-conservative (characteristic) form as

$$\tilde{\mathbf{D}}_{\text{NS}}\frac{\partial\tilde{\mathbf{Q}}_{\text{NS}}}{\partial t} + \tilde{\mathbf{A}}_{\text{NS}}\frac{\partial\tilde{\mathbf{Q}}_{\text{NS}}}{\partial\xi} + \tilde{\mathbf{B}}_{\text{NS}}\frac{\partial\tilde{\mathbf{Q}}_{\text{NS}}}{\partial\eta} + \tilde{\mathbf{C}}_{\text{NS}}\frac{\partial\tilde{\mathbf{Q}}_{\text{NS}}}{\partial\zeta}$$

$$= \frac{\partial}{\partial\xi}\left(\frac{\tilde{\mathbf{D}}_{\text{NS}}}{J}g_{ij}\frac{\partial J\tilde{\mathbf{Q}}_{\text{NS}}}{\partial\xi}\right) + \frac{\partial}{\partial\eta}\left(\frac{\tilde{\mathbf{D}}_{\text{NS}}}{J}g_{ij}\frac{\partial J\tilde{\mathbf{Q}}_{\text{NS}}}{\partial\eta}\right)$$

$$+ \frac{\partial}{\partial\zeta}\left(\frac{\tilde{\mathbf{D}}_{\text{NS}}}{J}g_{ij}\frac{\partial J\tilde{\mathbf{Q}}_{\text{NS}}}{\partial\zeta}\right) + \tilde{\mathbf{S}}_{\text{NS}}. \quad (32)$$

For the sake of clarity of derivation of the characteristic boundary conditions, we will treat the problem as if all physical properties for both liquid and solid are those of the liquid phase and as if they are constant. Then, the eigenmatrix $\tilde{\mathbf{\Lambda}}_{\text{NS}}$ corresponding to the flux vector Jacobian coefficient matrix $\tilde{\mathbf{A}}_{\text{NS}}$ is

$$\tilde{\mathbf{\Lambda}}_{\text{NS}} = \text{diag}\,[U-a, U+a, U, U, U] \quad (33)$$

where a is the equivalent local speed of sound

$$a = (U^2+\beta(\xi_{,x}^2+\xi_{,y}^2+\xi_{,z}^2))^{1/2}. \quad (34)$$

From the eigenvalues it is obvious that there are four incoming characteristics corresponding to four positive eigenvalues. Thus, four variables (u, v, w, θ) have to be specified at the inlet assuming that ζ is in the direction of the mean flow there. Nevertheless, the first eigenvalue is negative at the inlet meaning that one variable, p, has to be computed at the inlet from a characteristic form of the equations. Similarly, at the exit boundary, the pressure should be specified while the velocity components and the temperature should be obtained by integrating the characteristic equations.

Coefficients of the similarity transformation matrix $\mathbf{M}_{\text{NS}\xi}^{-1}$ that converts the ξ-direction generalized flux vector $\tilde{\mathbf{E}}_{\text{NS}}$, into its characteristic non-conservative form are given by

$$m_{11} = -U-a \quad m_{12} = \xi_{,x} \quad m_{13} = \xi_{,y}$$

$$m_{14} = \xi_{,z} \quad m_{15} = 0 \quad (35)$$

$$m_{21} = -U+a \quad m_{22} = \xi_{,x} \quad m_{23} = \xi_{,y}$$

$$m_{24} = \xi_{,z} \quad m_{25} = 0 \quad (36)$$

$$m_{31} = \beta((\xi_{,y}k_{23}-\xi_{,z}k_{12})u+(\xi_{,z}k_{31}-\xi_{,x}k_{23})v$$

$$+ (\xi_{,x}k_{12}-\xi_{,y}k_{31})w)$$

$$m_{32} = U(k_{12}w-k_{23}v) - \beta(\xi_{,y}k_{23}-\xi_{,z}k_{12})$$

$$m_{33} = U(k_{23}u-k_{31}w) - \beta(\xi_{,z}k_{31}-\xi_{,x}k_{23})$$

$$m_{34} = U(k_{31}v-k_{12}u) - \beta(\xi_{,x}k_{12}-\xi_{,y}k_{31})$$

$$m_{35} = 0 \quad (37)$$

$$m_{41} = \beta((\xi_z k_{23} - \xi_y k_{31})u + (\xi_x k_{31} - \xi_z k_{12})v$$
$$+ (\xi_y k_{12} - \xi_x k_{23})w)$$

$$m_{42} = U(k_{31}v - k_{23}w) - \beta(\xi_z k_{23} - \xi_y k_{31})$$

$$m_{43} = U(k_{12}w - k_{31}u) - \beta(\xi_x k_{31} - \xi_z k_{12})$$

$$m_{44} = U(k_{23}u - k_{12}v) - \beta(\xi_y k_{12} - \xi_x k_{23})$$

$$m_{45} = 0 \tag{38}$$

$$m_{51} = (U^2 - a^2)\theta \quad m_{52} = -\xi_x U\theta$$

$$m_{53} = -\xi_y U\theta \quad m_{54} = -\xi_z U\theta \quad m_{55} = a^2 \tag{39}$$

where

$$k_{12} = \xi_z^2 - \xi_x \xi_y \quad k_{23} = \xi_x^2 - \xi_y \xi_z \quad k_{31} = \xi_y^2 - \xi_z \xi_x. \tag{40}$$

If equations (14) are pre-multiplied by the similarity transformation matrix $\mathbf{M}_{NS\xi}^{-1}$, the characteristic form of the equations is obtained. The equation corresponding to the negative eigenvalue is to be selected at the inlet, while at the exit the equations corresponding to the positive eigenvalues are chosen. The selection procedure can be conducted using the selection matrix $\mathbf{L}_{NS}$. If the boundary condition vector is $\mathbf{\Omega}_{NS}$ then

$$\mathbf{\Omega}_{NS}^{t+1} = \mathbf{\Omega}_{NS}^t + \frac{\partial \mathbf{\Omega}_{NS}}{\partial \tilde{\mathbf{Q}}_{NS}} \Delta \tilde{\mathbf{Q}}_{NS} \tag{41}$$

or

$$\frac{\partial \mathbf{\Omega}_{NS}}{\partial \tilde{\mathbf{Q}}_{NS}} \Delta \tilde{\mathbf{Q}}_{NS} = -\mathbf{\Omega}_{NS}^t. \tag{42}$$

Equations (42) are added to the system of transformed equations, so that,

$$\left[\mathbf{L}_{NS} \mathbf{M}_{NS\xi}^{-1} + \frac{\partial \mathbf{\Omega}_{NS}}{\partial \tilde{\mathbf{Q}}_{NS}} \right] \Delta \tilde{\mathbf{Q}}_{NS}$$
$$= -\alpha_k \Delta t \left[\mathbf{M}_{NS\xi}^{-1} \tilde{\mathbf{R}}_{NS}^{k-1} + \frac{\mathbf{\Omega}_{NS}^t}{\alpha_k \Delta t} \right]. \tag{43}$$

Here, t is the iteration level, α_k are the coefficients in the Runge–Kutta k-stage time-stepping scheme, and $\tilde{\mathbf{R}}_{NS}$ is the residual vector of system (14). At the inlet plane,

$$\mathbf{L}_{NS} = \text{diag}[1, 0, 0, 0, 0] \tag{44}$$

$$\mathbf{\Omega}_{NS} = [0, u - u_p, v - v_p, w - w_p, \theta - \theta_p]^T. \tag{45}$$

At the exit plane

$$\mathbf{L}_{NS} = \text{diag}[0, 1, 1, 1, 1] \tag{46}$$

$$\mathbf{\Omega}_{NS} = [\bar{p} - \bar{p}_p, 0, 0, 0, 0]^T \tag{47}$$

so that

$$\frac{\partial \mathbf{\Omega}_{NS}}{\partial \tilde{\mathbf{Q}}_{NS}} = \text{diag}[\beta J, 0, 0, 0, 0]. \tag{48}$$

Nevertheless, the characteristic boundary conditions

at the exit plane require specification of the melt pressure on the entire exit plane, which cannot be performed correctly since the correct pressure distribution there is unknown a priori especially if the flow at the exit is not fully developed. A remedy is to use a different type of exit boundary conditions.

Non-reflecting exit flow boundary conditions

The non-reflecting boundary conditions do not force us to specify any of the physical variables at the exit plane thus allowing computation to capture variable pressure distribution at the exit plane. Instead of specifying the exit plane pressure as required by the characteristic boundary condition treatment, an additional equation needs to be solved when using the non-reflecting boundary formulation. Specifically, the non-reflecting boundary condition demands that the amplitude of an incoming wave be constant in time [12, 19–21] so that the outgoing waves depend only on information at the boundary and within the domain. Thus, those equations which represent outgoing waves can be solved at the exit boundary as they are to give three velocity components and temperature at the exit. At the inlet boundary, a characteristic boundary treatment was employed.

For one-dimensional problems, wave propagation direction is well defined. For multi-dimensional problems, there is no unique direction of propagation because the coefficient matrices $\tilde{\mathbf{A}}_{NS}$, $\tilde{\mathbf{B}}_{NS}$, $\tilde{\mathbf{C}}_{NS}$ cannot be simultaneously diagonalized. Boundary condition analysis requires that any one coordinate direction be diagonalizable at a time. Eigenvectors corresponding to the Jacobian coefficient matrix $\tilde{\mathbf{A}}$ are solutions of the matrix equation $[\tilde{\mathbf{A}}_{NS} - \tilde{\lambda}_{NS}\mathbf{I}]\{\mathbf{x}\} = 0$. Pre-multiplying the governing equation (14) with the inverse of a similarity matrix $\tilde{\mathbf{S}}_{NS}$ of $\tilde{\mathbf{A}}_{NS}$ gives

$$\tilde{\mathbf{S}}_{NS}^{-1} \tilde{\mathbf{D}}_{NS} \frac{\partial \tilde{\mathbf{Q}}_{NS}}{\partial t} + \tilde{\mathbf{S}}_{NS}^{-1} \tilde{\mathbf{A}}_{NS} \tilde{\mathbf{S}}_{NS} \tilde{\mathbf{S}}_{NS}^{-1} \frac{\partial \tilde{\mathbf{Q}}_{NS}}{\partial \xi}$$
$$+ \tilde{\mathbf{S}}_{NS}^{-1} \tilde{\mathbf{H}}_{NS} = 0 \tag{49}$$

where

$$\tilde{\mathbf{H}}_{NS} = \tilde{\mathbf{B}}_{NS} \frac{\partial \tilde{\mathbf{Q}}_{NS}}{\partial \eta} + \tilde{\mathbf{C}}_{NS} \frac{\partial \tilde{\mathbf{Q}}_{NS}}{\partial \zeta} - \tilde{\mathbf{S}}_{NS}$$

$$- \frac{\partial}{\partial \xi}\left(\frac{\tilde{\mathbf{D}}_{NS}}{J} g_{ij} \frac{\partial J\tilde{\mathbf{Q}}_{NS}}{\partial \xi} \right) - \frac{\partial}{\partial \eta}\left(\frac{\tilde{\mathbf{D}}_{NS}}{J} g_{ij} \frac{\partial J\tilde{\mathbf{Q}}_{NS}}{\partial \eta} \right)$$

$$- \frac{\partial}{\partial \zeta}\left(\frac{\tilde{\mathbf{D}}_{NS}}{J} g_{ij} \frac{\partial J\tilde{\mathbf{Q}}_{NS}}{\partial \zeta} \right). \tag{50}$$

Then we can define a column vector $\mathbf{L}_{NS}$ as follows

$$\mathbf{L}_{NS} = \tilde{\mathbf{S}}_{NS}^{-1} \tilde{\mathbf{A}}_{NS} \tilde{\mathbf{S}}_{NS} \tilde{\mathbf{S}}_{NS}^{-1} \frac{\partial \tilde{\mathbf{Q}}_{NS}}{\partial \xi}. \tag{51}$$

Components of $\mathbf{L}_{NS}$ defined as above are used for the equations corresponding to the outgoing waves, while for the equations corresponding to incoming waves the characteristic boundary treatment and non-reflecting boundary treatment have different

approaches. In characteristic boundary treatment for incoming waves, flow properties are specified instead of solving the equations. On the other hand, the non-reflecting boundary treatment defines Ls differently for only these equations corresponding to incoming waves [19, 20]

$$L_i = -(\tilde{\mathbf{S}}_{NS}^{-1}\tilde{\mathbf{H}}_{NS})_i. \tag{52}$$

Here the subscript 'i' represents the equation corresponding to the incoming wave. This condition constrains the amplitude of the incoming wave to remain constant with time so that the outgoing waves are not allowed to reflect back into the domain. This formulation of non-reflecting exit boundary condition was used in the present work allowing for automatic prediction of non-uniform pressure on the exit plane.

The system of the magnetic field equations (28) is also hyperbolic in time. The eigenvalues of the Jacobian matrix of this system are $\tilde{\Lambda}_{MAG} = \text{diag}[U, U, 0]$ in the case of ξ-direction. At the inlet plane, therefore, two components of the magnetic field vector should be specified, while the axial component H_x of the magnetic field vector has to be evaluated from the characteristic equation. The transformation matrix for the magnetic transport equations is given by

$$\mathbf{M}_{MAG\xi}^{-1} = \begin{bmatrix} k_{23}v - k_{12}w & k_{31}w - k_{23}u & k_{12}u - k_{31}v \\ k_{23}w - k_{31}v & k_{31}u - k_{12}w & k_{12}v - k_{23}u \\ -\xi_{,x}k_{123} & -\xi_{,y}k_{123} & -\xi_{,z}k_{123} \end{bmatrix}$$

$$\tag{53}$$

where k_{12}, k_{23}, k_{31} are defined in equation (40) and

$$k_{123} = k_{12} + k_{23} + k_{31} \tag{54}$$

$$\mathbf{L}_{MAG} = \text{diag}[1, 1, 0] \tag{55}$$

$$\Omega_{MAG} = \{H_x - H_{xp}, H_y - H_{yp}, 0\}^T. \tag{56}$$

At the exit plane, all three magnetic field components were continuously updated by integrating the governing equations.

NUMERICAL RESULTS

Based on the elaborated analytical model and the numerical algorithm, a fully three-dimensional MHD flow analysis computer code has been developed [6]. Numerical results from this code were compared with known analytical solutions and proved to be highly accurate [6]. This code was then augmented to incorporate thermally induced buoyancy, temperature-dependent physical properties of the melt and the solid phase and the effects of latent heat release with a model for the mushy region [7–12].

Two basic configurations were studied with this code: a cubicial closed container (Fig. 1(a)) with sides of length $l = 0.01$ m and a straight duct having square cross sections (Fig. 1(b)) with dimensions 0.01 m × 0.01 m × 0.0475 m. The cubical closed container was completely filled with the melt and the duct was

assumed to be horizontal with the melt flowing in the positive x-direction. Gravity was assumed to act vertically downward in the z-direction. If not indicated otherwise, the solid walls were thermally insulated. All runs were performed with CFL number 2.8, von Neuman number 0.4, artificial compressibility parameter $\beta = 5$ and with the coefficient of fourth order artificial [18] dissipation $v = 0.0001$. The values of the reference parameters were: $v_0 = 0.01$ m s^{-1}, $l_0 = 0.01$ m, $g_0 = 9.81$ m s^{-2} and the exponent used in the model for latent heat release (equation (2)) was $n = 5$. To account for the rapidly increasing viscosity in the mushy region and to treat the solid phase as an extremely viscous fluid, we used $\eta_{0s}/\eta_{0l} = 10^n$. All computations were performed in FORTRAN language on a Cray-YMP computer using a single processor. A typical computation time with a magnetic field was approximately one hour.

Case 1. Closed container without solidification

As a basic test of the capability and accuracy of the computer code to predict three-dimensional buoyancy driven flows without phase change we used the test case of Ozoe and Okada [3] for a cubical closed container filled with molten silicon (Table 1). A computational grid consisting of $30 \times 30 \times 10$ cells symmetrically clustered towards the walls was used for this purpose. They presented computational results at three perpendicular mid-planes with $Ra = 10^6$ and $Pr = 0.054$. Two numerical tests were carried out in the cubical enclosure with one of the vertical walls ($x^* = 0$) uniformly heated ($\theta = 0.5$) and the opposite vertical wall ($x^* = 1.0$) uniformly cooled ($\theta = -0.5$). Notice that in this test case we used Ozoe and Okada's formulation that $\theta = (T - T_0)/(T_{hot} - T_{cold})$ with $T_0 = (T_{hot} + T_{cold})/2$, while both T_{hot} and T_{cold} were assumed greater than $T_{liquidus}$. The first test run was performed without an external magnetic field ($Ht = 0$) and the second with an external uniform magnetic field ($Ht = 500$) applied horizontally in the x-direction. In the case of no magnetic field the computed isotherms on the horizontal $z^* = 0.5$ mid-plane (Fig. 2(a)) and on the vertical $y^* = 0.5$ mid-plane (Fig. 2(b)) compare well with the computational results (Fig. 2(c), (d)) of Ozoe and Okada [3]. In the case with the magnetic field applied, the computed isotherms (Fig. 3(a), (b)) compare reasonably well (Fig. 3(c), (d)) with those of Ozoe and Okada. This

Table 1. Non-dimensional input parameters

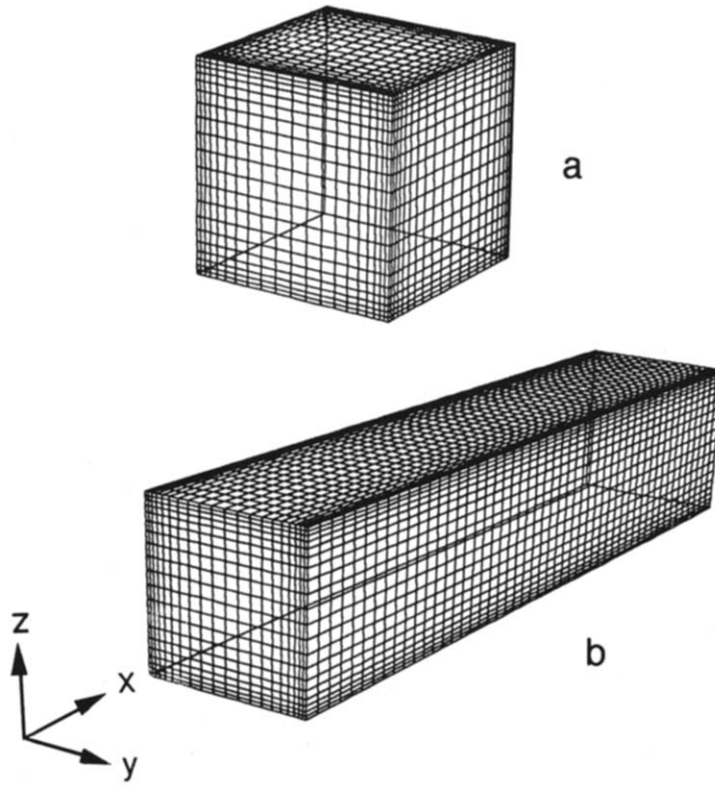|	Steel melt	Silicon melt
Re	100	200
Pr	0.4167	0.054
Gr	1000	1.85×10^7
Ec	5.56×10^{-10}	7.87×10^{-8}
Ht	0, 10, 30	0, 500
P_m	0.01	0.01

Fig. 1. Test configurations and computational grids: (a) closed container, (b) straight square cross section duct.

case is indicative of suppression of flow circulation by the strong externally applied magnetic field and the dominance of conduction in the process of heat transfer. Consequently, the magnetic field thickens the thermal boundary layer in the horizonal mid-plane $z^* = 0.5$ (Figs. 2(a) and 3(a)) and also in the vertical mid-plane $y^* = 0.5$ (Figs. 2(b) and 3(b)).

Case 2. Closed container with solidification from the top

In this case the cubical closed container was filled with the molten steel (Table 1 and Table 2) having its top wall ($z^* = 0$) uniformly cooled below freezing temperature ($\theta = -1$) so that significant solidification occurs at the upper wall [22]. The bottom wall ($z^* = 1.0$) was uniformly heated ($\theta = 1$). The container was discretized with $20 \times 20 \times 20$ grid cells that were clustered symmetrically towards the walls. Two cases were run without the influence of the magnetic field ($Ht = 0$). One of the cases was in reduced gravity ($g = 0.01g_0$) and the other with the full influence of gravity. Evidently, in the reduced gravity case conduction is the dominant mode of heat transfer (Fig. 4(a)), whereas in the full gravity case heat transfer is carried out by both conduction and thermal convection (Fig. 4(b)). The computed isotherms (Fig. 5(a)) in full gravity and the corresponding contours of constant z-velocity components (Fig. 5(b)) on the

horizontal $z^* = 0.5$ mid-plane indicate strong centrally located downward jet and upward motion close to the walls thus forming a deformed toroidal melt motion.

Case 3. Closed container with side solidification

A cubical closed container (Fig. 1(a)) was discretized with $20 \times 20 \times 20$ symmetrically clustered grid cells and assumed filled with molten silicon (Table 3 and Table 4) having the values of the reference quantities: $v_0 = 0.02269$ m s^{-1}, $l_0 = 0.01$ m, $\Delta T = 37.5$ K, $\rho_0 = 2550$ kg m^{-3}, $c_0 = 1059$ J kg^{-1} K^{-1}, $k_0 = 64$ W m^{-1} K^{-1}, $T_0 = 1685$ K, $\mu_0 = 7.018 \times 10^{-4}$ kg m^{-1} s^{-1}, $\sigma_0 = 4.3 \times 10^4$ W^{-1} m^{-1} and $g_0 = 9.81$ m s^{-2}. It should also be pointed out that the values of c, k and μ were varied linearly within the mushy region. Notice (Table 3) that we

Table 2. Physical properties used for molten steel

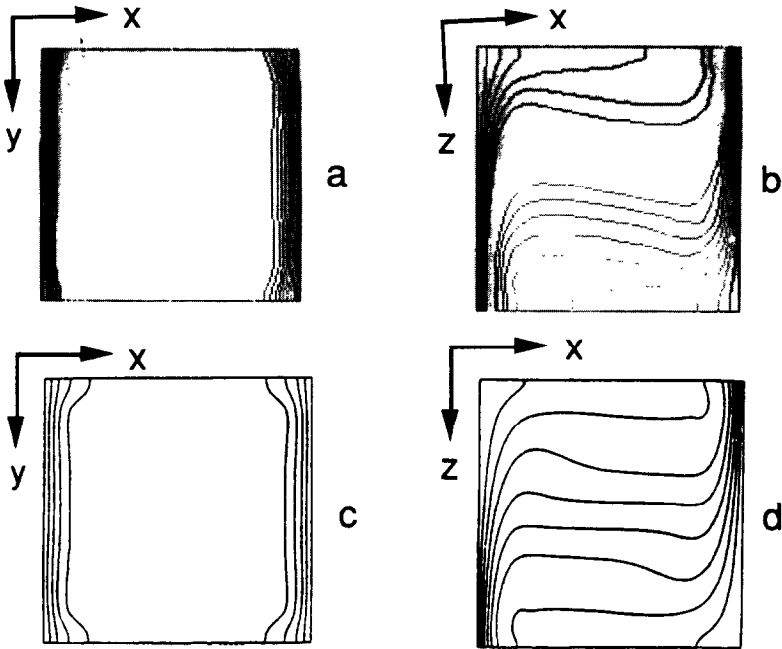|	
C_{pl} [J kg^{-1} K^{-1}]	788
C_{ps} [J kg^{-1} K^{-1}]	$465.4 + 0.1336T$
k_l [W m^{-1} K^{-1}]	12.29
k_s [W m^{-1} K^{-1}]	8.16
T_l [K]	1727
T_s [K]	1670
L [J kg^{-1}]	265 200

FIG. 2. Container without solidification (side cooling); isotherms for $Ht = 0$ with: (a) $z^* = 0.5$ computed; (b) $y^* = 0.5$ computed; (c) $z^* = 0.5$ from [3]; (d) $y^* = 0.5$ from [3].
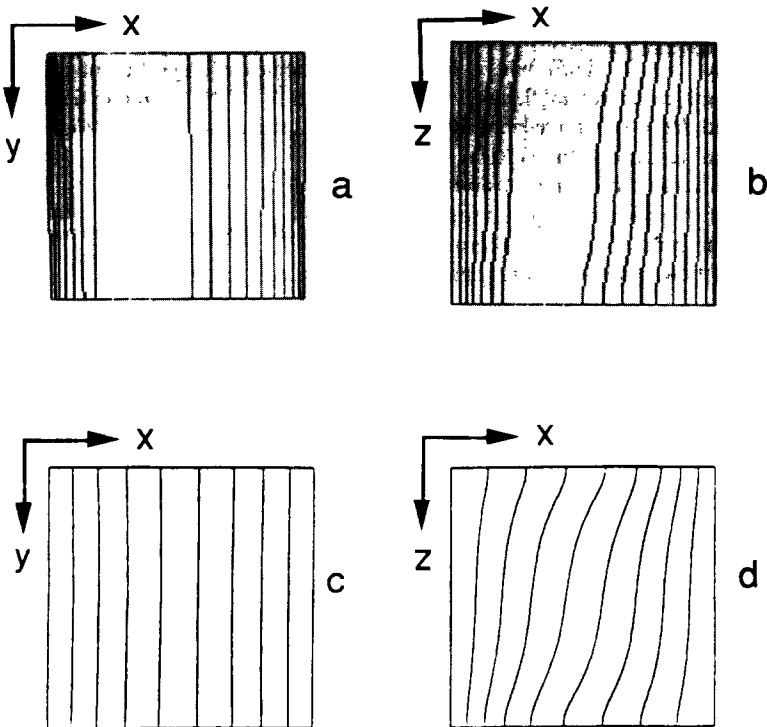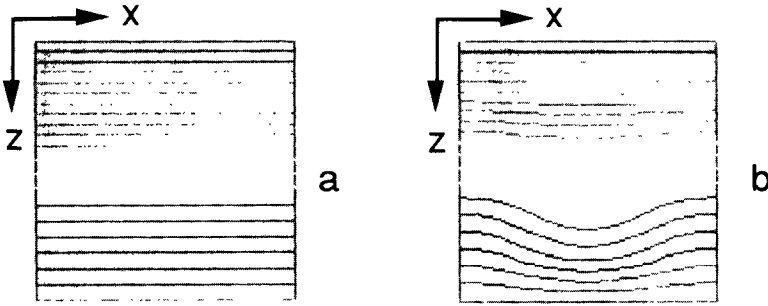

FIG. 3. Container without solidification (side cooling); isotherms for $Ht = 500$ with: (a) $z^* = 0.5$ computed; (b) $y^* = 0.5$ computed; (c) $z^* = 0.5$ from [3]; (d) $y^* = 0.5$ from [3].

Fig. 4. Container with top solidification; isotherms for $y^* = 0.5$ and $Ht = 0$ with: (a) $g = 0.01g_0$; (b) $g = g_0$.
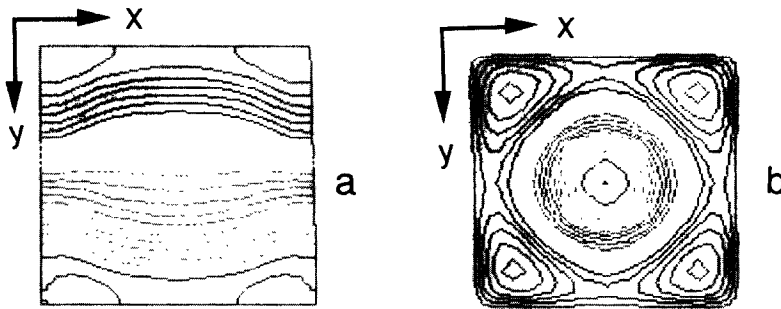
Fig. 5. Container with top solidification ($z^* = 0.5$, $g = g_0$, $Ht = 0$): (a) isotherms; (b) constant z-velocity contours.

have assumed that the magnetic permeability coefficient for silicon is one order of magnitude larger than for vacuum. Consequently, the Hartmann number in our case becomes $Ht = 418.6B_0$ where B_0 is the magnetic field strength measured in Teslas. In all pertinent cases, we used $Ht = 100$ corresponding to $B_0 = 0.2389$ Tesla. In all test cases, the vertical wall at $x^* = 0$ was kept uniformly hot ($\theta = 2$) and the opposite vertical wall ($x^* = 1$) was kept uniformly cold ($\theta = -1$), with the remaining walls thermally insulated. Uniform gravity was applied in the negative

z-direction in all the test cases (Fig. 1(a)). The following is a discussion of the computational results obtained by orienting a uniform steady external magnetic field along different axes. Depending on the orientation of the magnetic field, a different amount of solid phase has accrued (Fig. 6) in each of the test cases.

Table 3. Physical properties used for silicon

ρ_l [kg m^{-3}]	2550
ρ_s [kg m^{-3}]	2330
c_l [J kg^{-1} K^{-1}]	1059
c_s [J kg^{-1} K^{-1}]	1038
k_l [W m^{-1} K^{-1}]	64
k_s [W m^{-1} K^{-1}]	22
T_l [K]	1685
T_m [K]	1683
T_s [K]	1681
μ [kg m^{-1} s^{-1}]	7.018×10^{-4}
α [K^{-1}]	1.4×10^{-4}
L [J kg^{-1}]	1 803 000
σ_l [W^{-1} m^{-1}]	12.3×10^5
σ_s [W^{-1} m^{-1}]	4.3×10^4
γ [Tm A^{-1}]	$4\pi \times 10^{-6}$

Table 4. Non-dimensional parameters used for silicon

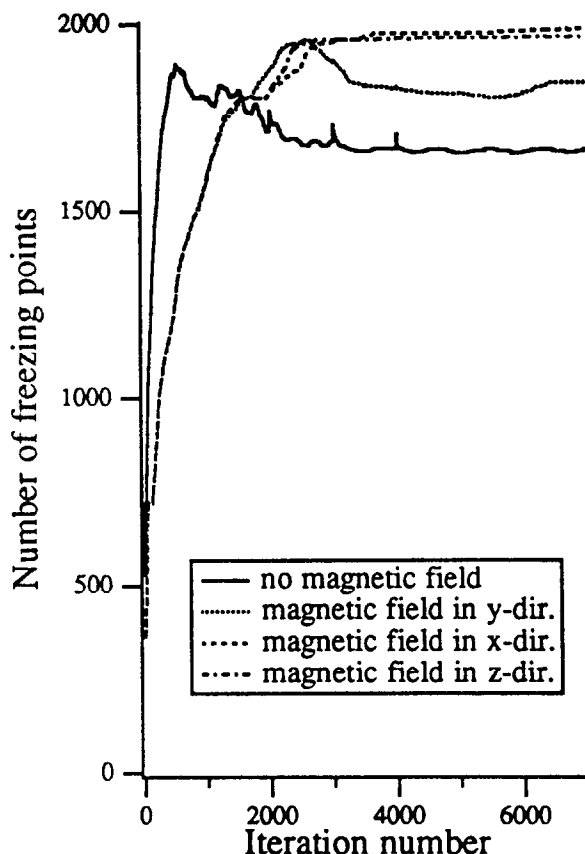| Non-dimensional numbers	Values used
$Re = \dfrac{\rho_0 v_0 l_0}{\mu_0}$	824.6
$Fr = \dfrac{v_0}{(g_0 l_0)^{1/2}}$	0.007047
$Gr = \dfrac{\rho_0^2 \alpha_0 g_0 l_0^3 \Delta T_0}{\mu_0^2}$	67.99×10^4
$Ec = \dfrac{v_0^2}{c_0 \Delta T_0}$	1297×10^{-8}
$Pr = \dfrac{\mu_0 c_0}{k_0}$	0.01161
$P_m = \dfrac{\gamma_0 \sigma_0 \mu_0}{\rho_0}$	4.255×10^{-6}
$Ht = \gamma_0 l_0 H_0 \left(\dfrac{\sigma_0}{\mu_0}\right)^{1/2}$	$418.6B_0$

FIG. 6. Container with side solidification: convergence histories for the four cases.

Case 3.1. Closed container side solidification with no magnetic field. Comparison of the computed isotherms (Fig. 7(a)) and the velocity vector field (Fig. 7(b)) in the vertical mid-plane ($y^* = 0.5$) depict strong melt circulation and the solid that accrued on the cold wall ($x^* = 1$). The liquid/solid interface is highly curved in this plane. There are strong thermal gradients and 1666 solidified cells accrued on the cold vertical wall. Similarly, computed isotherms (Fig. 7(c)) in the horizontal mid-plane ($z^* = 0.5$) show that the thermal gradients inside the solid are significant and that the solid/liquid shape does not vary significantly in the y-direction.

Case 3.2. Close container solidification with magnetic field in y-direction (perpendicular to plane of recirculation). Computed isotherms (Fig. 8(a)) in the vertical mid-plane ($y^* = 0.5$) when compared with the isotherms in the case without the magnetic field (Fig. 7(a)) appear to be less curved and the vertical thermal boundary layer is thicker. As expected, the computed velocity vector field (Fig. 8(b)) in the same plane is clearly weaker than the computed velocity field in the case without the magnetic field (Fig. 7(b)). Consequently, the liquid/solid interface straightened somewhat and more solid accrued resulting in 1843 solidified cells. Since the magnetic field reduced melt

convection, the computed isotherms in the horizontal mid-plane ($z^* = 0.5$) show almost no variation (Fig. 8(c)) in the y-direction.

Case 3.3. Closed container solidification with magnetic field in x-direction (from hot to cold wall). The computed isotherms (Fig. 9(a)) in the vertical mid-plane ($y^* = 0.5$) when compared with the isotherms in the case with the magnetic field acting in y-direction (Fig. 8(a)) are significantly straightened. The magnetic field acting perpendicular to the hot and the cold vertical walls is definitely suppressing the melt motion (Fig. 9(b)) resulting in 1986 solidified cells and the melt/solid interface that is clearly less curved than in the previous test cases. The isotherms (Fig. 9(c)) computed in the horizontal mid-plane ($z^* = 0.5$) show that the temperature field is practically two-dimensional. Identical results were obtained when applying the field in negative x-direction. In both cases the magnetic field force was suppressing vertical velocity components and consequently slowing the overall circulation.

Case 3.4. Closed container solidification with magnetic field in negative z-direction (against gravity). The computed isotherms (Fig. 10(a)) in the vertical mid-plane ($y^* = 0.5$) are mildly curved as compared with the isotherms in the cases when the magnetic field was
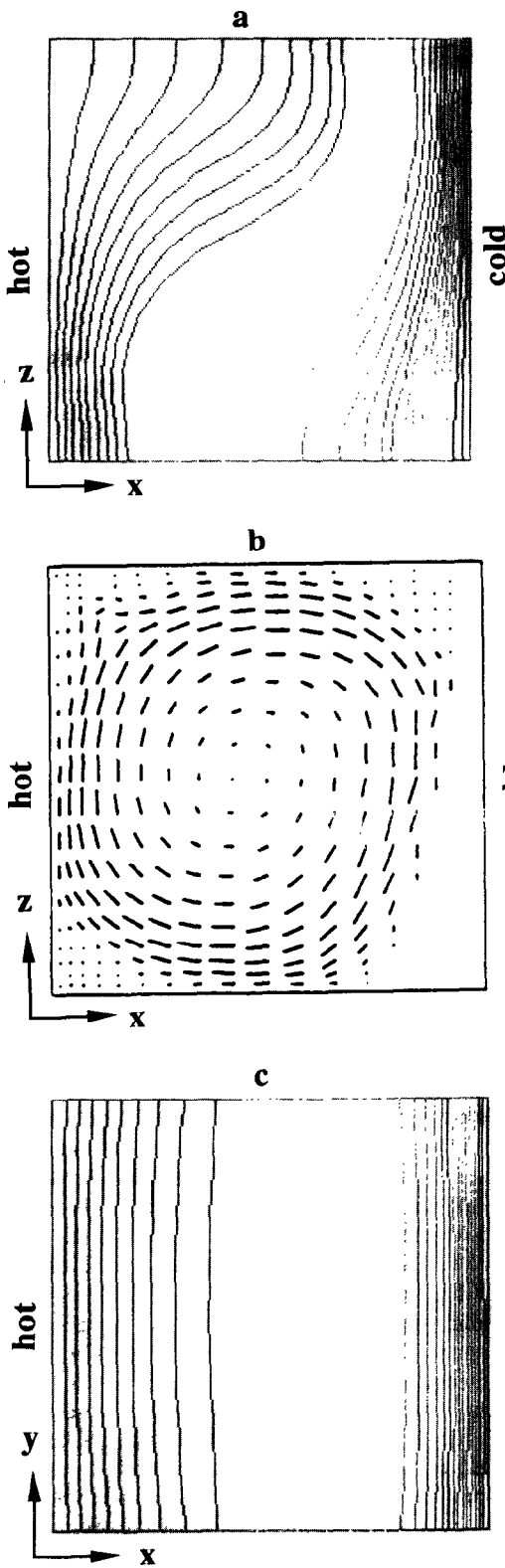
FIG. 7. Container with side solidification and no magnetic field: (a) isotherms in vertical $y^* = 0.5$ mid-plane; (b) velocity vectors in vertical $y^* = 0.5$ mid-plane; (c) isotherms in horizontal $z^* = 0.5$ mid-plane.
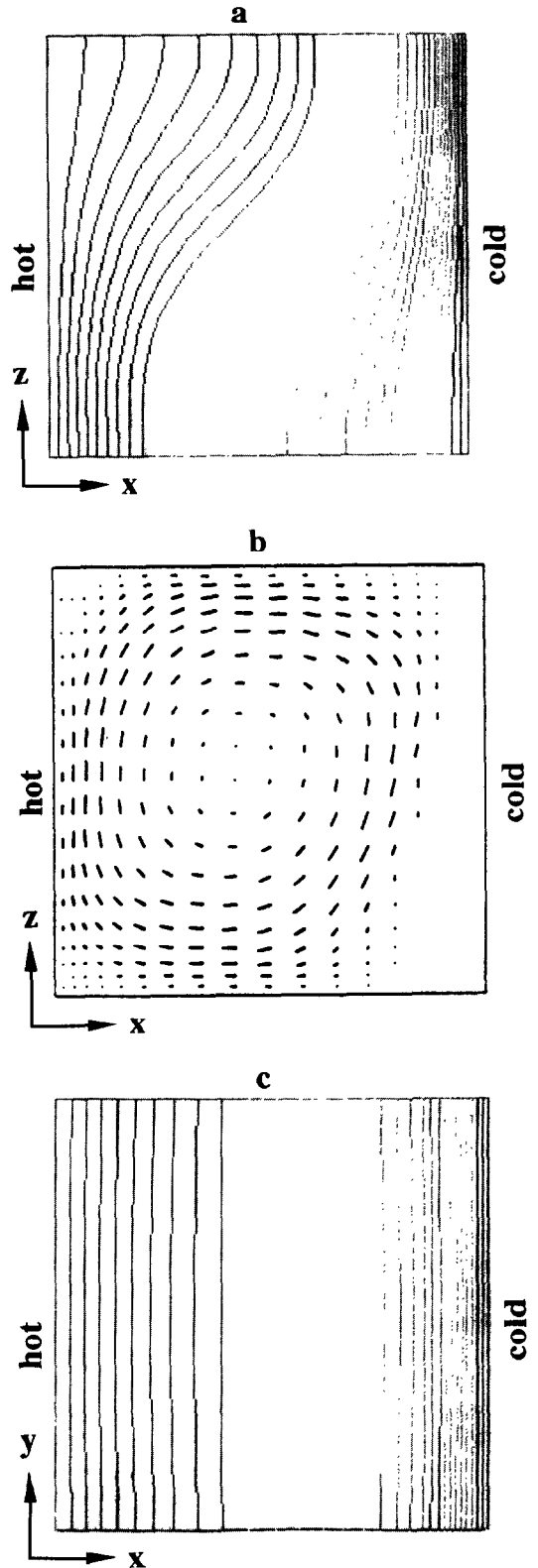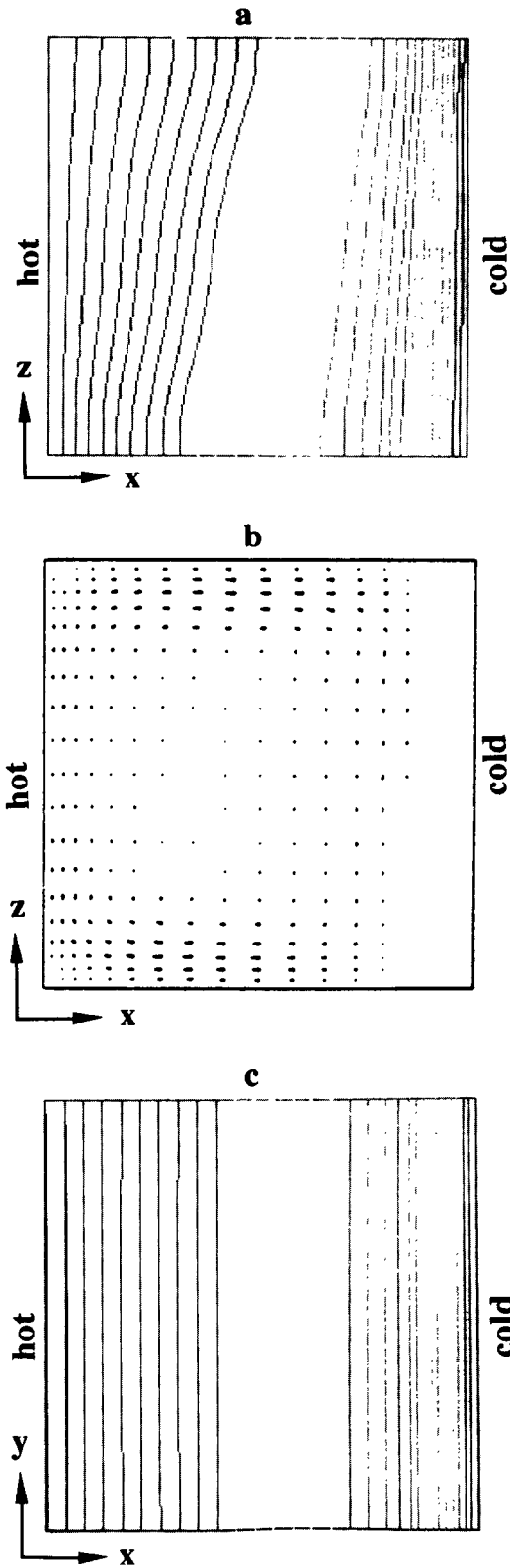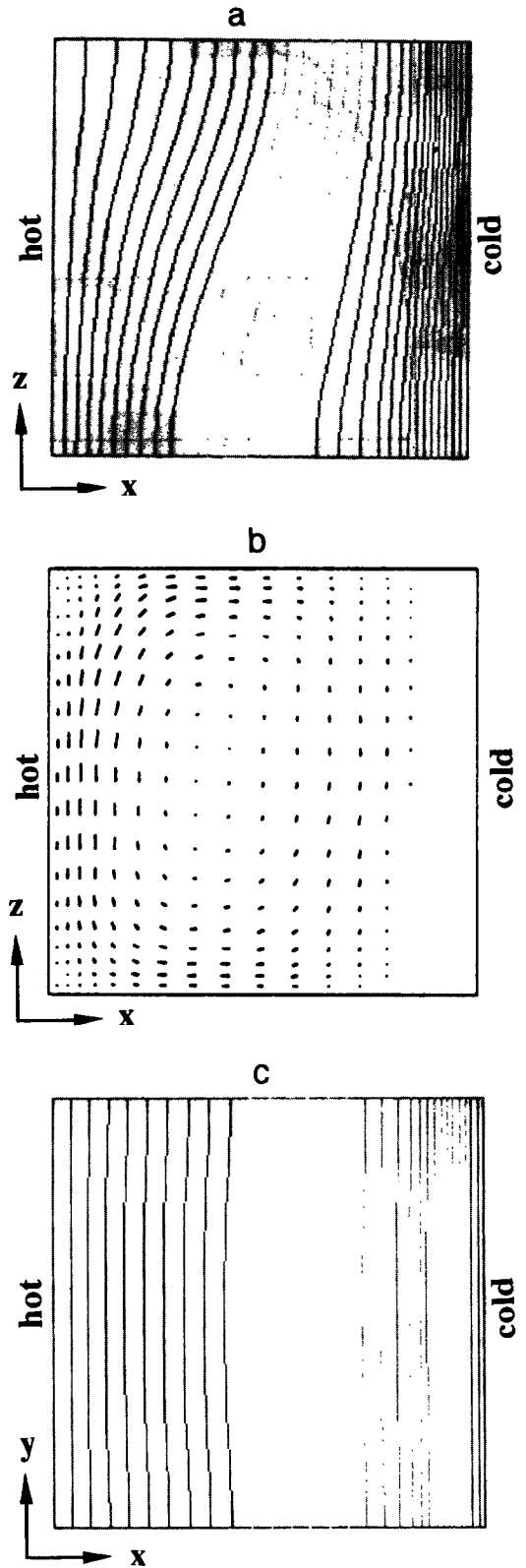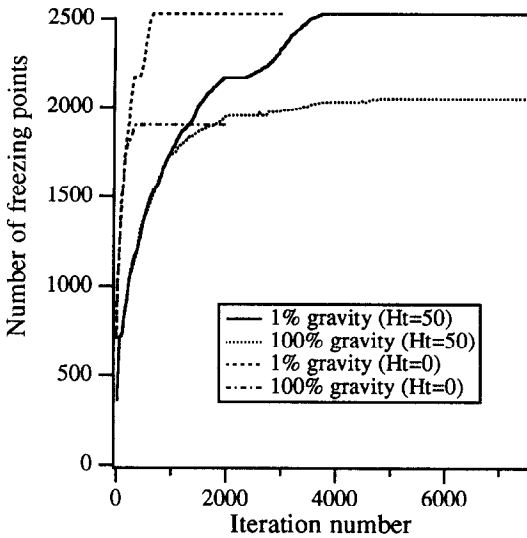
FIG. 8. Container with side solidification and a uniform magnetic field in y-direction: (a) isotherms in vertical $y^* = 0.5$ mid-plane; (b) velocity vectors in vertical $y^* = 0.5$ mid-plane; (c) isotherms in horizontal $z^* = 0.5$ mid-plane.

FIG. 9. Container with side solidification and a uniform magnetic field in positive x-direction: (a) isotherms in vertical $y^* = 0.5$ mid-plane; (b) velocity vectors in vertical $y^* = 0.5$ mid-plane; (c) isotherms in horizontal $z^* = 0.5$ mid-plane.

FIG. 10. Container with side solidification and a uniform magnetic field in positive z-direction: (a) isotherms in vertical $y^* = 0.5$ mid-plane; (b) velocity vectors in vertical $y^* = 0.5$ mid-plane; (c) isotherms in horizontal $z^* = 0.5$ mid-plane.

FIG. 11. Container with side solidification of molten steel:
convergence histories.

acting horizontally in *y*-direction (Fig. 8(a)) and in *x*-direction (Fig. 9(a)). The vertically upward magnetic field also suppresses the melt motion (Fig. 10(b)) and creates almost the same amount of solid on the cold vertical wall (1962 solidified cells) as in the case when the field was acting horizontally in the hot-to-cold direction. The computed isotherms (Fig. 10(c)) in the horizontal mid-plane ($z^* = 0.5$) show that the temperature field in the melt is mildly three-dimensional. Identical results were obtained when applying the field in the same direction as the gravity. In both cases the magnetic field force was suppressing horizontal velocity components and consequently slowing the overall circulation.

In addition, a number of numerical tests were performed where the container was filled with the molten steel. Solidification from a side wall was simulated with full and reduced gravity and with or without a uniform vertical magnetic field. Figure 11 summarizes the effects of the magnetic field and the gravity for these test cases. It is clear that the effect of the magnetic field is more pronounced (in this case it increases the amount of accrued solid) with the increase in gravity magnitude.

Straight duct flow with solidification

The second configuration studied was a straight three-dimensional duct with a square cross section. Uniform molten steel (Table 1 and Table 2) temperature ($\theta = 2$) was imposed at the duct inlet ($x^* = 0$). Along all four walls a cooling was arbitrarily specified as $\theta = 2 - 3.6 \sin(x^*\pi)$. Characteristic boundary conditions were used at the inlet, while specifying nothing at the exit. Instead, a non-reflecting boundary condition was enforced at the exit so that variable pressure at the exit plane can be correctly predicted. The flow field was discretized with $50 \times 20 \times 20$ grid cells that were clustered symmetrically towards the duct walls. Four computer runs were performed for this configuration.

The first test case represents a solidifying flow field in a reduced gravity environment ($g = 0.01g_0$) without any magnetic field ($Ht = 0$). Computed solidified zones are clearly evident on all four walls of the duct from the computed velocity vector fields (Fig. 12(a)) in the horizontal ($z^* = 0.5$) mid-plane and the isotherms (Fig. 12(b)) in the vertical ($y^* = 0.5$) mid-plane. For all practical purposes the solution is doubly symmetric with respect to the longitudinal mid-planes.

An additional test case was then run in a reduced gravity environment ($g = 0.01g_0$) with a uniform magnetic field of $Ht = 50$ acting vertically downward. The influence of the magnetic field is evident from the velocity vector plot (Fig. 13(a)) in the horizontal ($z^* = 0.5$) mid-plane depicting flattened velocity profiles. This leads to a slight decrease in the amount of solid accrued on the vertical walls (Fig. 13(b)).

An additional case was run with a full gravitational field ($g = g_0$) but without any magnetic field ($Ht = 0$).
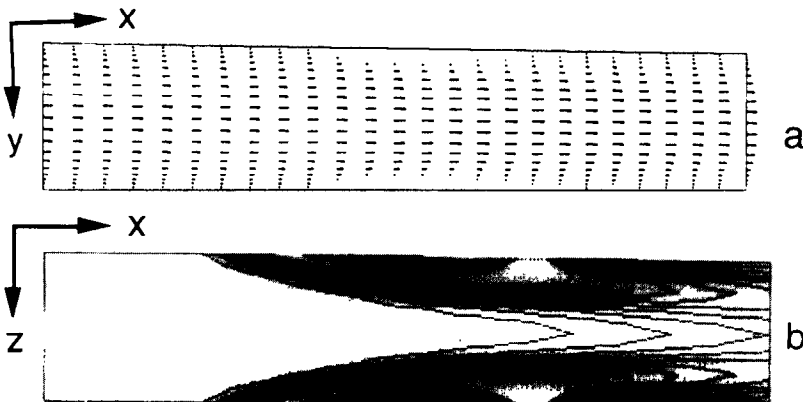

FIG. 12. Straight square cross section duct with solidification ($g = 0.01g_0$, $Ht = 0$): (a) velocity field at
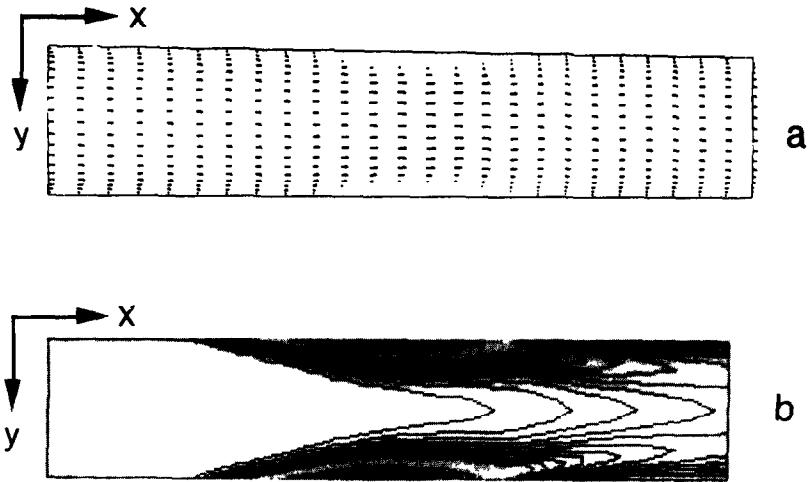$z^* = 0.5$; (b) isotherms at $y^* = 0.5$.

FIG. 13. Straight square cross section duct with solidification ($g = 0.01g_0$, $Ht = 50$): (a) velocity field at $z^* = 0.5$; (b) isotherms at $y^* = 0.5$.
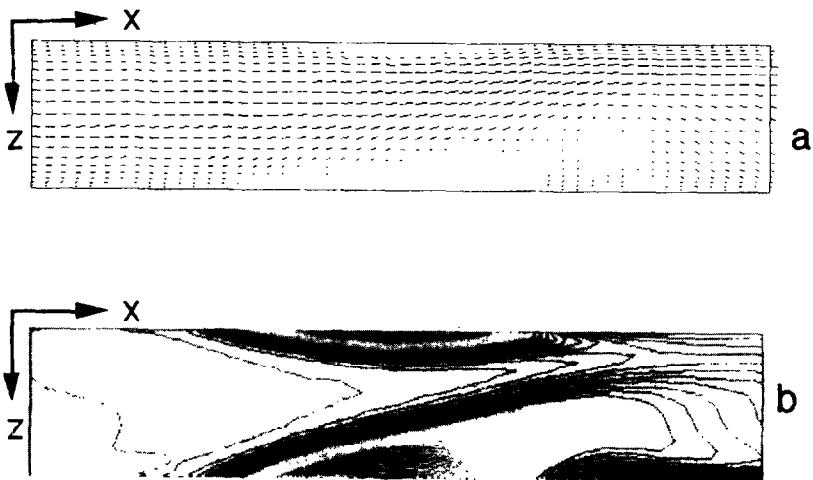

FIG. 14. Straight square cross section duct with solidification ($y^* = 0.5$, $g = g_0$, $Ht = 0$): (a) velocity field; (b) isotherms.
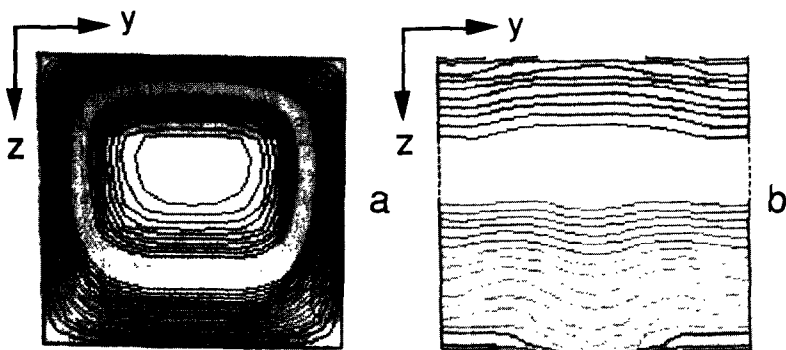

FIG. 15. Straight square cross section duct with solidification ($g = g_0$, $Ht = 0$): (a) velocity field at $x^* = 0.5$; (b) pressure at the exit ($x^* = 1.0$).

In this case strong asymmetry can be noticed in the vertical plane velocity pattern (Fig. 14(a)) and the computed isotherms (Fig. 14(b)). This is due to strong thermal buoyancy. In this case significantly more solid accrued on the bottom wall and less on the top wall as compared to the solid accretion on the side walls. This is also evident from the computed isotherms in the vertical cross section plane ($x^* = 0.5$) of the duct (Fig. 15(a)). The computed non-uniform pressure at the exit plane (Fig. 15(b)) clearly demonstrates the benefits of using non-reflecting boundary conditions rather than characteristic boundary conditions at the exit ($x^* = 1.0$).

CONCLUSIONS

A complete analytical and numerical formulation has been developed for the theoretical prediction of phase change processes inside three-dimensional arbitrarily shaped containers and ducts with and without the influence of an externally applied steady magnetic field and arbitrary gravity vector. Computational results confirm that the strength and the orientation of the magnetic field has a profound influence on the solidification and melting since it weakens flow recirculation regions and causes distorted velocity profiles having overshoots close to the solid boundaries. This change influences convective heat transfer and affects the amount of the solid phase accrued on undercooled walls. Consequently, the temperature field also changes under the influence of the external magnetic field. This demonstrates a possibility for the development of an active control algorithm for realistic three-dimensional solidification or melting that would be especially applicable to reduced gravity environments since it would require low strength magnetic fields.

REFERENCES

1. S. Chandrasekhar, *Hydrodynamic and Hydromagnetic Stability*. Dover, New York (1961).
2. O. M. Stuetzer, Magnetohydrodynamics and electrohydrodynamics, *Phys. Fluids* **5**(6), 534–544 (1962).
3. H. Ozoe and K. Okada, The effect of the direction of the external magnetic field on the three-dimensional natural convection in a cubical enclosure, *Int. J. Heat Mass Transfer* **32**, 1939–1954 (1989).
4. C. Vives, Effects of a magnetically forced convection during the crystallization in mould of aluminum alloys, *J. Crystal Growth* **94**, 739–750 (1989).
5. M. Salcudean and P. Sabhapathy, Numerical study of liquid encapsulated Czochralski growth of gallium arsenide with and without an axial magnetic field, *Symposium on Computer Modeling and Simulation of Manufacturing Processes* (Edited by B. Singh, Y. T. Im, I. Haque and C. Altan), ASME MD-Vol. 20, pp. 115–127, Book No. G00552 (1990).
6. S. Lee and G. S. Dulikravich, Magnetohydrodynamic steady flow computations in three dimensions, *Int. J. Numer. Meth. Fluids* **13**(8), 917–936 (1991).
7. B. Kosovic, G. S. Dulikravich and S. Lee, Freezing under the influence of a magnetic field: computer simulation, *Proceedings of ICHMT International Symposium on Macroscopic and Microscopic Heat and Mass Transfer in Biomedical Engineering*, Athens, Greece, 2–6 September 1991 (Edited by K. Diller and A. Shitzer), pp. 307–326. Elsevier Press, Amsterdam (1992).
8. G. S. Dulikravich, B. Kosovic and S. Lee, Solidification in reduced gravity with magnetic fields and temperature-dependent physical properties, *Symposium on Heat and Mass Transfer in Solidification Processing*, ASME WAM '91, Atlanta, Georgia, 1–6 December 1991 (Edited by S. G. Advani and C. Beckermann), HTD-Vol. 175/MD-Vol. 25, pp. 61–73 (1991).
9. G. S. Dulikravich and B. Kosovic, Solidification of variable property melts under the influence of low gravity, magnetic fields and electric fields, AIAA paper 92-0694, AIAA Aerospace Sciences Meeting, Reno, Nevada, 6–9 January (1992).
10. G. S. Dulikravich, B. Kosovic and S. Lee, Magnetized fiber orientation control in solidifying composites: numerical simulation, 28th ASME National Heat Transfer Conference, San Diego, California, 9–12 August 1992, *Symposium on Transport Phenomena in Materials Processing and Manufacturing* (Edited by M. Charmchi et al.), HTD-Vol. 196, pp. 135–144; also in *J. Heat Transfer* **115**, 255–262 (1993).
11. G. S. Dulikravich, V. Ahuja and S. Lee, Three-dimensional control of crystal growth using magnetic fields, SPIE paper 1916-07, *Proceedings of Smart Structures and Materials Conference*, Albuquerque, New Mexico, 1–4 February (1993).
12. G. S. Dulikravich, V. Ahuja and S. Lee, Three-dimensional solidification with magnetic fields and reduced gravity, AIAA paper 93-0912, Aerospace Sciences Meeting, Reno, Nevada, 11–14 January (1993).
13. D. D. Gray and A. Giorgini, The validity of the Boussinesq approximation for liquids and gases, *Int. J. Heat Mass Transfer* **19**, 545–551 (1976).
14. V. R. Voller and C. R. Swaminathan, General source-based method for solidification phase change, *Numer. Heat Transfer, Part B* **19**, 175–189 (1991).
15. D. Poirier and M. Salcudean, On numerical methods used in mathematical modeling of phase change in liquid metals, ASME paper 86-WAM/HT-22, Anaheim, California, 7–12 December (1986).
16. A. Chorin, A numerical method for solving incompressible viscous flow problems, *J. Comput. Phys.* **2**, 12–26 (1967).
17. S. Lee and G. S. Dulikravich, Performance analysis of DMR method for acceleration of iterative algorithms, AIAA paper 91-0241, AIAA Aerospace Sciences Meeting, Reno, Nevada, 7–10 January (1991).
18. A. Jameson, W. Schmidt and E. Turkel, Numerical solution of the Euler equations by finite volume methods using Runge–Kutta time-stepping scheme, AIAA paper 81-1259, AIAA Computational Fluid Dynamic Conference, Palo Alto, California, 20–22 June (1981).
19. K. W. Thomson, Time-dependent boundary conditions for hyperbolic systems, I, *J. Comput. Phys.* **68**, 1–24 (1987).
20. K. W. Thomson, Time-dependent boundary conditions

for hyperbolic systems, II, *J. Comput. Phys.* **89**, 439–461 (1990).

21. S. H. Reitsma and V. P. Manno, Non-reflective boundary conditions for fluid-acoustic simulations using a finite volume formulation, ASME Fluids Engineering Conference, Washington, D.C. 21–24 June, *Symposium on Computational Aero- and Hydro-Acoustics, ASME FED*-Vol. 147, pp. 71–82 (1993).

22. R. C. Kerr, A. W. Woods, M. G. Worster and H. E. Huppert, Solidification of an alloy cooled from above. Part 1: Equilibrium growth, *J. Fluid Mech.* **216**, 323–342 (1990).